Supporting Information

Kailun Deng [a], Cui Jiwei[a], Chenhe Wu[a] , Zhaohong Han[a], Lequan Liu [a] and Jinhua Ye[ab].*

[a]Advanced Catalytic Materials Research Center, School of Materials Science and Engineering; State Key Laboratory of Precious Metal Functional Materials, Tianjin University, Tianjin, 300072, China.

[b]ntenational Center for Materials Nanoarchitectonics (WPI-MANA), National Institute for Materials Science (NIMS), Tsukuba, 305-0044, Japan.

**Corresponding Authors.*

E-mail address: Lequan.Liu@tju.edu.cn

Preparation of $BiVO_4$ (BVO) photoanode.

The first step was to prepare BiOI grown on the cleaned fluorine-doped tin oxide (FTO). 30 mM $Bi(NO_3)_2$ (Aladdin, 99%) was dissolved in 400 mM KI (Aladdin, 99%) aqueous solution (50 mL). The pH was adjusted to 1.8 using dilute HNO_3 (Sinopharm, 99%) to form a clear red-orange solution (Solution A). Then, 100 mM p-benzoquinone (Sinopharm, 99%) was added to absolute ethanol (20 mL) to obtain solution B. Mix A and B with vigorous stirring for a few minutes for the dark black plating solution. The FTO substrate (2*1 cm^2) was used as the working electrode (WE), the platinum foil was used as the counter electrode (CE), and the Ag/AgCl electrode in a saturated KCl solution was used as a reference electrode (RE) to form a 3-electrode system. Prior to electrodeposition, the FTO was blown dried with Ar. Given a constant voltage of -0.15 V vs. Ag/AgCl ($V_{Ag/AgCl}$) for 7 mins at room temperature, the deposition area was 1 cm^2, then the obtained BiOI electrode was rinsed with deionized water and blown dry with Ar. The second step was to convert BiOI to $BiVO_4$. A 200 mM solution of vanadium acetylacetonate (Aladdin, 99%) in dimethyl sulfoxide (Rionlon, 99%) was prepared, and 0.2 mL of the solution was drop-cast onto the BiOI electrode. The coated substrate was annealed at 723 K for 2 h with a ramping rate of 2 K min^{-1} in air. The resulting film was then immersed in a 1 M NaOH solution and gently stirred for 30 min, followed by rinsing with deionized water to obtain a bright yellow $BiVO_4$.

Preparation of $BiVO_4$/an-TiO_2 (BVO/an-TiO_2) photoanode.

A total of 20 mL of deionized water was placed in a beaker and cooled to 273 K using an ice-water bath. Then, 200 μL of $TiCl_3$ solution (Aladdin, 20%) was added dropwise

under stirring until a homogeneous dispersion was obtained. Upon removal, the $BiVO_4$ photoanode initially appeared black; it was left to stand for 10 min until the surface returned to yellow, followed by rinsing with deionized water and drying under an Ar flow. Finally, the photoanode was annealed at 200 °C for 30 min to yield the $BiVO_4/TiO_2$ sample.

Preparation of $BiVO_4$/am-TiO_2 (BVO/am-TiO_2) photoanode.

The synthesis of $BiVO_4$/am-TiO_2 photoanode is similar to that of $BiVO_4$/an-TiO_2, and no further calcination or thermal treatment is required after washing and drying.

Preparation of $BiVO_4$/FeOOH/NiOOH (BVO/FeOOH/NiOOH) photoanode.

To load the FeOOH/NiOOH OECs, a FeOOH layer was first photodeposited on $BiVO_4$ followed by the photodeposition of NiOOH. Photodeposition of FeOOH on the $BiVO_4$ electrode was carried out in a 0.1 M $FeSO_4$ (Aladdin, 99%) solution while gently stirring. Prior to the photodeposition of FeOOH, the solution was purged with Ar for 30 min. An undivided three-electrode cell was used, which was composed of a $BiVO_4$ WE, a Pt CE, and a Ag/AgCl (3.5 M KCl) RE. AM 1.5 G was used as the light source. To facilitate photodeposition, an external bias of ca. 0.25 $V_{Ag/AgCl}$ (3.5 M KCl) was applied for 90 s. After photodeposition, an electrodeposition of FeOOH was carried out in the same solution by applying +1.2 $V_{Ag/AgCl}$ (3.5 M KCl) for 1 min. This was to deposit FeOOH on any bare $BiVO_4$ or FTO surfaces exposed to the electrolyte. The same procedure used for the photodeposition of NiOOH was used except for the plating solution, which was a 0.1 M $NiSO_4$ (Aladdin, 99%) solution with pH adjusted to 6.5-7.2 by carefully adding NaOH. To facilitate photodeposition, an external bias of ca.

0.11 $V_{Ag/AgCl}$ (3.5 M KCl) was applied for 30s. After the photodeposition, electrodeposition of NiOOH was carried out by applying +1.2 $V_{Ag/AgCl}$ (3.5 M KCl) for 1 min in the same solution.

Preparation of $BiVO_4$/an-TiO_2/FeOOH/NiOOH (BVO/an-TiO_2/FeOOH/NiOOH) and $BiVO_4$/am-TiO_2/FeOOH/NiOOH (BVO/am-TiO_2/FeOOH/NiOOH) photoanodes.

The cocatalysts were loaded onto BVO/an-TiO_2 and BVO/am-TiO_2 using the same method via photoelectrochemical deposition, with charge amounts of 45 mC/cm^2 for FeOOH and 22 mC/cm^2 for NiOOH, respectively.

Preparation of Ta_2O_5. nH_2O.

Amorphous Ta_2O_5•nH_2O were fabricated based on the synthesis of Na_3TaO_4 and $Na_8[Ta_6O_{19}]$. Briefly, 1.10 g of Ta_2O_5 and 1 g of NaOH were thoroughly mixed and then transferred into an alumina crucible and calcined at 723 K for 15 h in air. The resulting solid was subsequently dissolved in 125 mL H_2O by sonication and vigorous magnetic stirring, giving an aqueous solution of $Na_8[Ta_6O_{19}]$ and NaOH with a pH of approximately 12. The pH of this solution was then adjusted to 6 by adding a 0.5 M aqueous H_2SO_4 solution. In this process, the $[Ta_6O_{19}]^{8-}$ anions were protonated, underwent polymerization, and then were decomposed into Ta_2O_5•nH_2O. The white precipitate obtained from this process was washed with pure water to remove residual Na_2SO_4, and then dried overnight at 333 K under vacuum.

Preparation of Ta_3N_5.

Ta_2O_5. nH_2O was loaded into a quadrate alumina crucible and heated at 1173 K for 6 h

under a 100 mL min^{-1} flow of NH_3. The aimed photocatalysts were obtained after rinsing and overnight drying of the resulting solids at 333 K under vacuum.

Preparation of Ta_3N_5 photoanode.

Typically, 3 mg of Ta_3N_5 was dispersed in 1 mL ethanol and 40 μL Nafion solution to form a suspension, which was sprayed onto F-doped tin oxide (FTO) glass using an airbrush on a hot plate maintained at 353 K. For each electrode, a total spraying volume of 400 μL was applied to a defined 1 × 1 cm^2 area on the FTO substrate, which served as the working electrode.

Electrodeposition of CoOOH cocatalyst.

A Co-containing catalyst was electrodeposited from a solution of 0.01 M cobalt(II) nitrate hexahydrate (Aladdin, 99%) in a three-electrode electrochemical cell, while a Ag/AgCl reference electrode and a Pt counter electrode were used as the reference and counter electrodes, respectively. The deposition was performed by a multi-step potentiostatic method. On the basis of linear sweep voltammetric data, a nucleation step was conducted by applying -1.05 $V_{Ag/AgCl}$ for 5 s to initialize the formation of small seed particles, followed by a slower crystal growth step during the 10 s at a less negative potential of -0.85 $V_{Ag/AgCl}$. After electrodeposition, the electrodes were rinsed with deionized water and dried in a N_2 atmosphere.

Photoelectrochemical measurements.

The photoelectrochemical (PEC) properties of the samples were tested in a three-electrode system under AM 1.5 G simulated sunlight (100 mW cm^{-2}) on working station CHI 760E. The sample grown on the FTO substrate was used as the working electrode

(WE), the platinum sheet was used as the counter electrode (CE), and the Ag/AgCl (saturated KCl) electrode as reference electrode. The buffer was 1 M potassium borate solution (pH = 9.5). Linear scanning voltammetry tests were performed at 0-1.23 V vs reversible hydrogen electrode (E_{RHE}) at a rate of 20 mV/s. All potentials here were converted with the formula:

$$E_{RHE} = E_{Ag/AgCl} + 0.197 + 0.0591*pH$$

where $E_{Ag/AgCl}$ was the potential obtained by Ag/AgCl reference electrode. In the presence or absence of 0.2 M Na_2SO_3, Na_2SO_3 oxidation and water oxidation are performed. Electrochemical impedance spectroscopy (EIS) was tested under lighting conditions at 0.7 V_{RHE}.

Theory of PEC photoelectrodes.

According to previous theories, the water oxidation current density J_{H2O} is determined by the product of J_{abs}, η_{sep} and η_{trans}. When the electrolyte is changed to 1M K-B_i buffer containing 0.2 M Na_2SO_3, η_{trans} at this time theoretically becomes 100%, thus the charge-transfer efficiency (η_{trans}) is obtained by dividing the photocurrent for water oxidation (J_{H_2O}) by that for sulfite oxidation ($J_{Na_2SO_3}$)

$$\eta_{trans} = \frac{J_{H_2O}}{J_{Na_2SO_3}} \quad \text{(S1)}$$

The applied bias photon-to-current efficiency (ABPE) for water splitting was calculated from the following equation:

$$ABPE(\%) = \left[\frac{J(mA/cm^2) \times (1.23 - V_{bias})(V)}{P_{in}(mW/cm^2)}\right] AM\ 1.5G \times 100\% \quad \text{(S2)}$$

Where J represents the photocurrent density given by the workstation, V_{bias} represents

given voltage, P_{in} represents the power of the solar simulator, which is 100 mW cm^{-2}.

The incident photon-to-electron conversion efficiency (IPCE) was measured using a monochromator connected to a three-electrode system. The IPCE spectra were recorded in the wavelength range of 350-600 nm with a wavelength step of 10 nm under monochromatic illumination. The photocurrent density was collected at 1.23 VRHE after reaching a steady state at each wavelength. The IPCE values were calculated according to the following equation:

$$IPCE(\%) = \frac{J \times 1240}{\lambda \times P_{in}} \times 100\% \quad \text{(S3)}$$

where J represents the steady-state photocurrent density under monochromatic light at 1.23 V_{RHE}, λ represents the wavelength of monochromatic light, and P_{in} represents the incident light power density measured at the electrode surface.

Fabrication of Integrated ($BiVO_4$||Ta_3N_5)-Si tandem cell.

$BiVO_4$ and Ta_3N_5 photoanodes were bonded using conductive silver paste, with the spacing between the two electrodes controlled at approximately 1 mm to form the $BiVO_4$||Ta_3N_5 composite photoanode. The composite photoanode was electrically connected to the positive terminal of the Si solar cell using a copper wire and conductive silver paste, while a Pt foil cathode was connected to the negative terminal of the Si solar cell in the same manner. The Si solar cell was fixed to the backside of the $BiVO_4$||Ta_3N_5 composite photoanode with epoxy resin, which was also applied to encapsulate and insulate all electrical connections from the electrolyte. The geometric active area of the integrated tandem device was 15 cm^2.

PEC H_2 and O_2 evolution measurements.

Using Ar as a carrier gas, the amounts of H_2 and O_2 gases evolved from the PEC cell were analyzed using a gas chromatograph (GC-8A with TCD, Shimadzu). Light source and electrolyte were the same as those used for above PEC measurements, and the gas products were sampled every 1 hour.

Characterizations.

The crystal structure of the catalyst was characterized by X-ray diffraction (XRD; MiniFlex600) equipped with Cu Kα radiation at 40 kV and 200 mA at a scanning rate of 10 °/min. The morphology of the catalyst was observed by scanning electron microscope (SEM; S-4800, Hitachi, Japan). Transmission electron microscope (TEM; Tecnai G2 F20 FEI, U.S.A.) was used for the lattice analysis. The atomic scale lattice space was measured through Aberration-corrected scanning transmission electron microscopy (JEM-ARM200F, JEOL, Japan). The Raman spectra were recorded on Raman spectrometer (XploRa, HORIBA Scientific, USA) equipped with a green laser of 532 nm. X-ray photoelectron spectrum (XPS; ESCALAB-250Xi) is used to measure the chemical state of the catalyst surface elements, and the binding energy was referenced to C 1s peaks (284.8 eV) of contaminated carbon. Photoluminance spectra (PL; Horiba Jobin Yvon Fluorolog) was used for electron lifetime with the excitation light at 420 nm. The ultraviolet–visible diffuse reflectance spectra (UV–vis DRS; Shimadzu UV-2700) was used to study the optical performance. Fourier transform infrared (FTIR) spectroscopy was performed using Nicolet 6700 (Thermo SCIENTIFIC, USA). X-ray photoelectron spectroscopy (XPS) measurement was performed on Escalab 250 (Thermo Scientific, USA), using monochromatic Al Kα

radiation and C 1s peak (284.8 eV) as a reference. Steady-state fluorescence measurements and transient fluorescence were carried out on a fluorescence spectrophotometer (Fluorolog-3, HORIBA Scientific, USA) with an excitation wavelength of 360 nm and 390 nm, respectively.

Estimation of Film Thickness from XPS Measurements

The film thickness (d) was estimated based on the attenuation of the substrate signal intensity according to the following equation:

$$d = \lambda \cos\theta \ln\left(\frac{I_0}{I}\right) \tag{S4}$$

where λ is the effective attenuation length (EAL) of the substrate photoelectrons in the overlayer, θ is the photoelectron take-off angle with respect to the sample surface normal (typically 90° for normal emission), I_0 is the XPS peak intensity of the substrate without an overlayer, and I is the measured substrate intensity after overlayer deposition.

In cases where film density differs from the tabulated IMFP reference material, a correction was applied using the ratio of material densities to ensure accurate thickness estimation:

$$d_{corrected} = d \times \frac{\rho_{reference}}{\rho_{film}} \tag{S5}$$

In which $\rho_{reference}$ is the reference density associated with the IMFP source and ρ_{film} is the actual film density. In this work, the effective attenuation length λ was estimated using the TPP-2M formula. The calculated thickness provides an approximate value of the overlayer film, assuming a uniform and continuous coverage.

Calculation of Theoretical Solar-to-hydrogen Efficiency of BiVO4||Ta3N5 photoanode

The theoretical STH efficiency of the $BiVO_4$||Ta_3N_5 tandem photoanode under AM 1.5G illumination was calculated based on the maximum attainable photocurrent density, following established detailed-balance and tandem-absorber optical models.[1-3] The UV–vis absorption spectra of $BiVO_4$ and Ta_3N_5 were first converted to absorptance using

$$\alpha(\lambda) = 1 - 10^{-A(\lambda)} \tag{S6}$$

where $A(\lambda)$ is the measured absorbance. For the tandem configuration, the total absorptance was determined by

$$\alpha_{tandem}(\lambda) = 1 - \left(1 - \alpha_{BVO}(\lambda)\right)\left(1 - \alpha_{Ta_3N_5}(\lambda)\right) \tag{S7}$$

which represents the probability that a photon is absorbed by at least one of the two photoanodes.

The AM 1.5G spectral irradiance was converted into the corresponding photon flux using

$$\Phi(\lambda) = \frac{I_{AM\ 1.5G}(\lambda)\lambda}{hc} \tag{S8}$$

Assuming that each absorbed photon generates one electron, the theoretical photocurrent density was obtained by integrating the absorbed photon flux over the usable spectral range:

$$= q \int_{\lambda_{min}}^{\lambda_{max}} \Phi(\lambda)\alpha_{tandem}(\lambda)d\lambda \tag{S9}$$

where q is the elementary charge.

The theoretical STH efficiency was then calculated according to

$$\eta_{STH,th} = \frac{J_{ph,th} \times 1.23\ V}{P_{in}} \quad \text{(S10)}$$

with P_{in} = 100 mW cm^{-2} for AM 1.5G illumination.

Hall effect measurement details Hall effect measurements

Hall effect measurements were performed using a van der Pauw configuration at room temperature (≈300 K). For accurate determination of the intrinsic transport properties, $BiVO_4$, $BiVO_4$/am-TiO_2, and $BiVO_4$/an-TiO_2 films were deposited onto insulating glass substrates under the same electrodeposition and annealing conditions used for the photoanodes. Four ohmic contacts were made at the sample corners using silver paste, and a perpendicular magnetic field of 0.5 T was applied during the measurements.

The Hall voltage was recorded under a constant applied current, and the Hall coefficient, carrier concentration, and carrier mobility were calculated following standard van der Pauw procedures. All samples exhibited n-type behaviour, in agreement with previous studies on $BiVO_4$-based semiconductors. The mobility values presented in Fig. 3d were obtained directly from these measurements and reflect the intrinsic transport properties of the respective films.

Table S1 Hall effect results for the BVO-based films at 300 K.

Sample	Temperature (K)	Resistivity (Ω·cm)	Mobility ($cm^2V^{-1}s^{-1}$)	Carrier concentration (cm^{-3})	Hall coefficient ($cm^3\ C^{-1}$)	f-factor
BVO	300	3.86E+04	1.42E+00	1.14E+14	-5.49E+04	9.02E-01
BVO/am-TiO_2	300	2.17E+04	1.53E+00	1.88E+14	-3.32E+04	9.16E-01
BVO/an-TiO_2	300	2.33E+03	4.78E+00	5.61E+14	-1.11E+04	9.97E-01

Time-resolved photoluminescence (TRPL) analysis

Time-resolved photoluminescence (TRPL) decay curves were collected for BVO, BVO/am-TiO_2, and BVO/an-TiO_2 under pulsed excitation at the emission maximum of $BiVO_4$. The decay profiles were fitted using a standard biexponential function:

$$I(t) = A_1 exp\left(-\frac{t}{\tau_1}\right) + A_2 exp\left(-\frac{t}{\tau_2}\right) \quad \text{(S11)}$$

where A_1 and A_2 are the pre-exponential factors, and τ_1 and τ_2 correspond to the fast and slow decay components, respectively. The fast component (τ_1) is associated with interfacial recombination processes that are strongly influenced by surface defect density and interfacial hole extraction efficiency, whereas the slow component (τ_2) represents bulk electron–hole recombination within $BiVO_4$.

The amplitude-weighted average lifetime $\tau_{average}$ was calculated according to:

$$\tau_{average} = \frac{A_1\tau_1^2 + A_2\tau_2^2}{A_1\tau_1 + A_2\tau_2} \quad \text{(S12)}$$

This definition captures the overall recombination dynamics and provides a reliable comparison among samples with distinct interfacial properties.

Comparison with $BiVO_4$ Photoanodes Prepared by Alternative Methods

According to previous reports, $BiVO_4$ photoanodes have been fabricated using various deposition techniques, including spray pyrolysis, sol-gel processing, and physical vapor deposition methods such as sputtering. Spray-pyrolyzed $BiVO_4$ films can exhibit good crystallinity after high-temperature annealing; however, their photoelectrochemical performance is often limited by the short carrier diffusion length of $BiVO_4$, which requires the use of relatively thin films or structural design strategies to alleviate bulk recombination losses[4]. In contrast, sol-gel derived films may suffer from increased

structural disorder and defect density due to solution-derived porosity, leading to enhanced charge recombination. Sputtering can produce dense and uniform $BiVO_4$ films with improved crystallinity, but the resulting photoanodes commonly remain constrained by low carrier mobility, while the method itself involves higher cost and limited scalability. Despite these differences in fabrication routes and film characteristics, $BiVO_4$ photoanodes prepared by different methods generally exhibit limited carrier mobility and short carrier diffusion lengths, indicating that photoelectrochemical performance is primarily constrained by the intrinsic electronic properties of $BiVO_4$ rather than the specific deposition technique. In this context, electrodeposition offers a practical balance between material quality, scalability, and compatibility with subsequent surface and interface engineering.

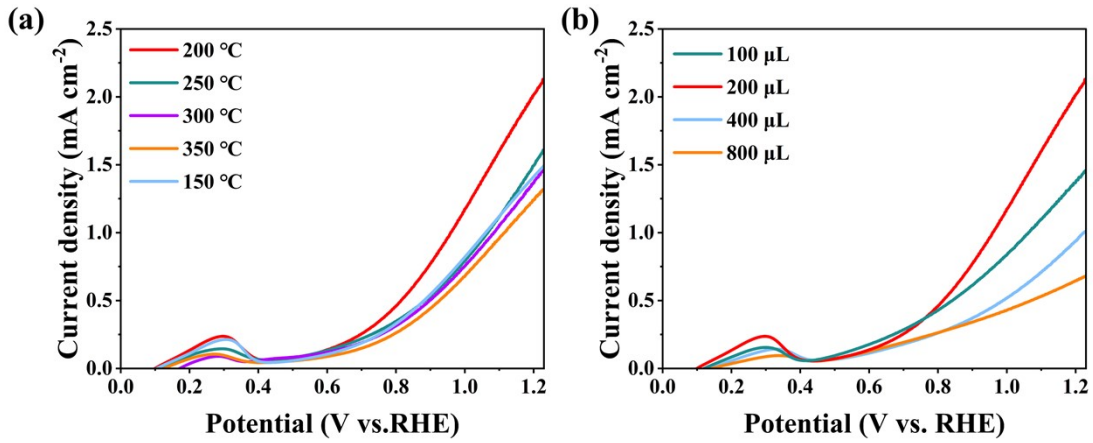

Figure S1 The synthesis parameters of the anatase TiO_2 layer. (a) Different annealing temperature (150, 200, 250, 300, and 350 ℃). (b) Different amounts of $TiCl_3$ solution (100, 200, 400, and 800 μL).

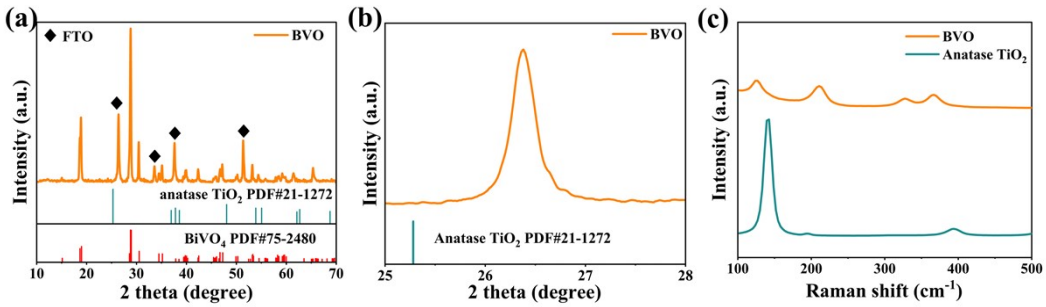

Figure S2 (a) XRD patterns, and (b) slow-scan XRD patterns of BVO (c) Raman spectra of BVO and anatase TiO_2.

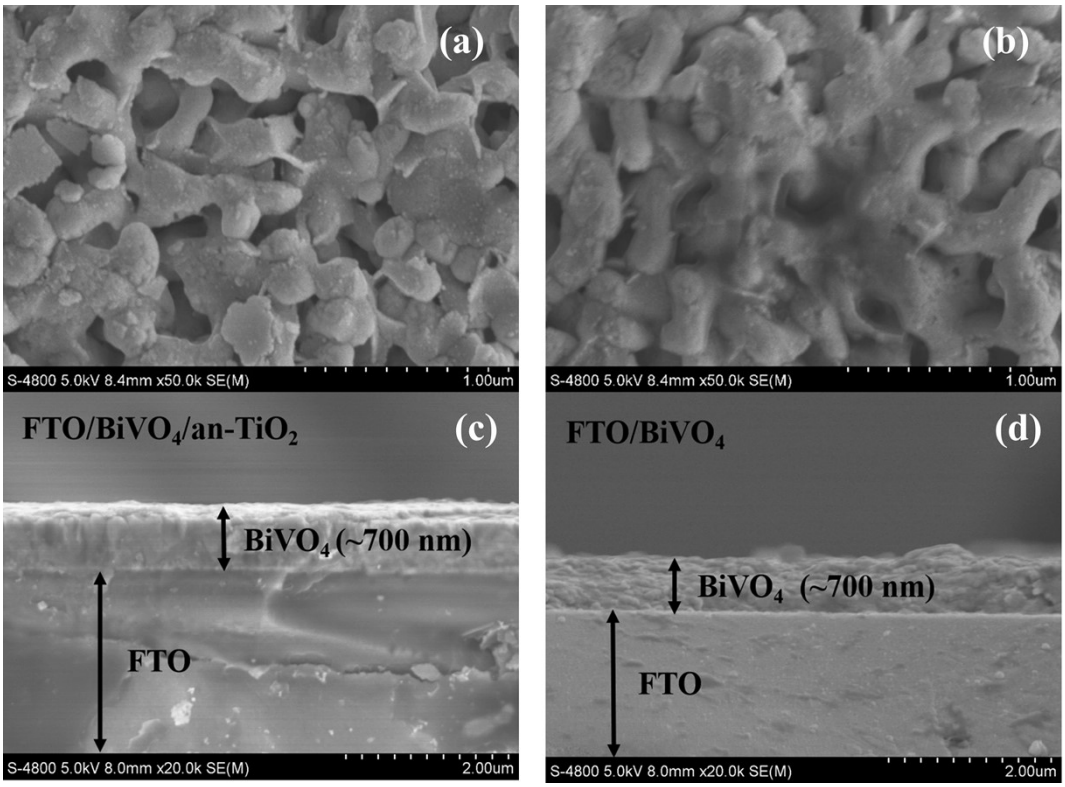

Figure S3 Top-view SEM images of (a) BVO/an-TiO_2 and (b) BVO/am-TiO_2.

Side lateral view SEM images of (c) BVO/an-TiO_2 and (d) BVO/am-TiO_2.

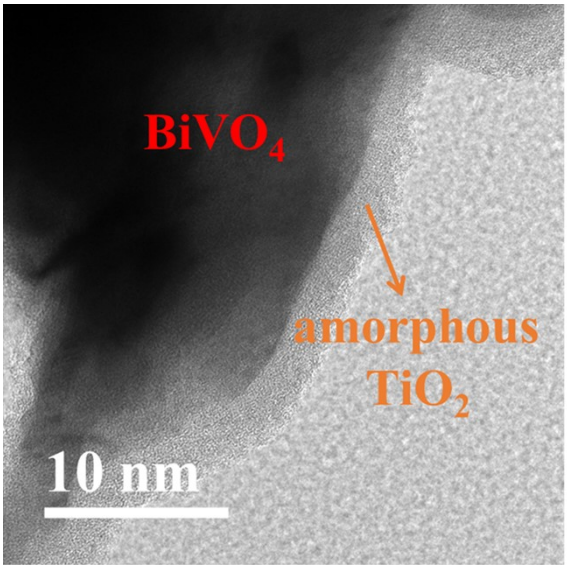

Figure S4 TEM image of the BVO/am-TiO_2 photoanode.

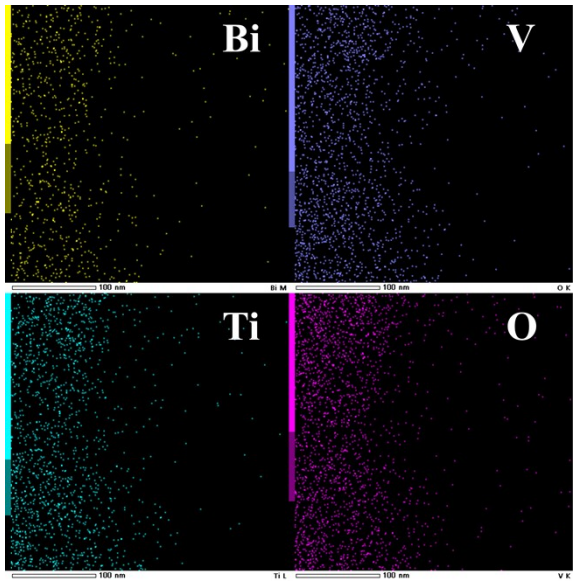

Figure S5 Elemental mapping images of BVO/an-TiO_2/FeOOH/NiOOH, showing the distributions of Bi, O, V, and Ti elements.

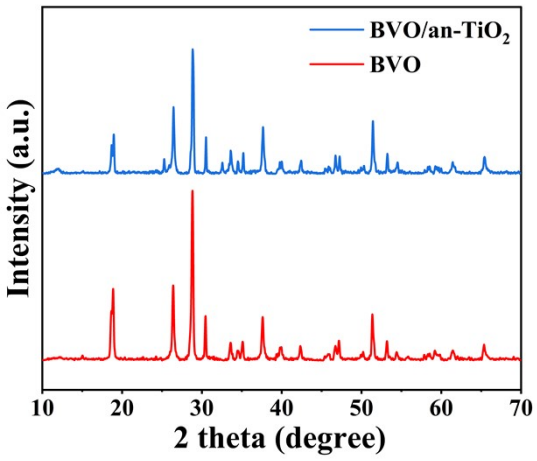

Figure S6 XRD results of BVO and BVO/an-TiO_2.

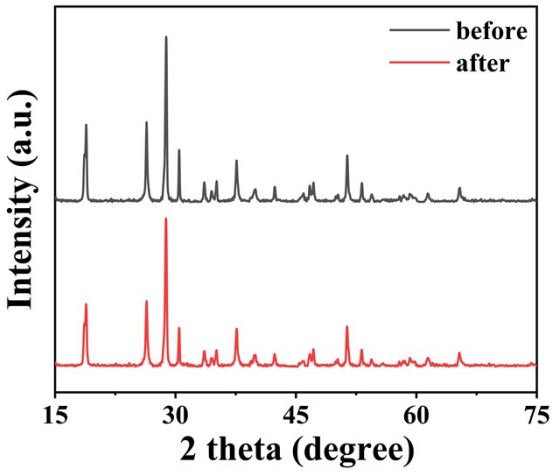

Figure S7 XRD patterns of BVO/an-TiO_2/FeOOH/NiOOH before and after the stability test.

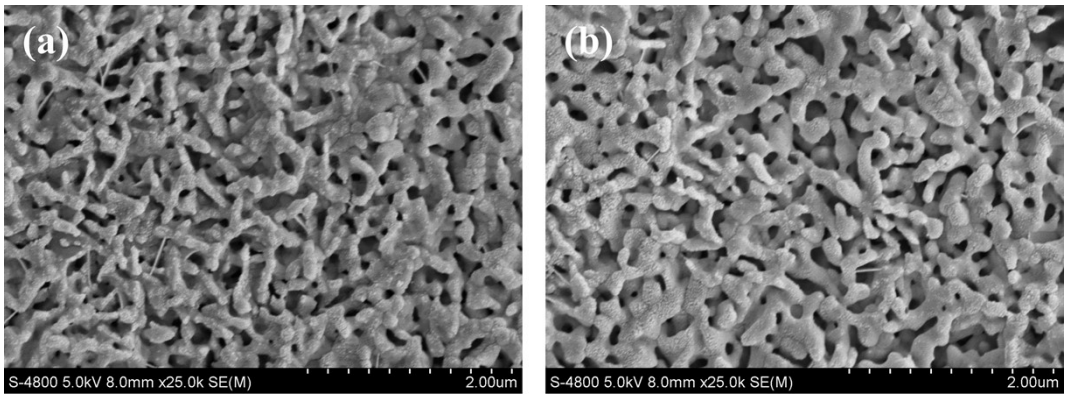

Figure S8 SEM of BVO/TiO_2/FeOOH/NiOOH (a) before and (b) after stability test.

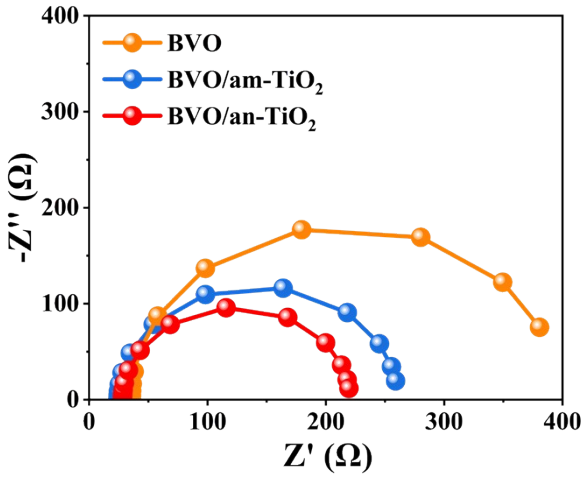

Figure S9 Electrochemical impedance spectra (EIS) measured at 0.7 V_{RHE}.

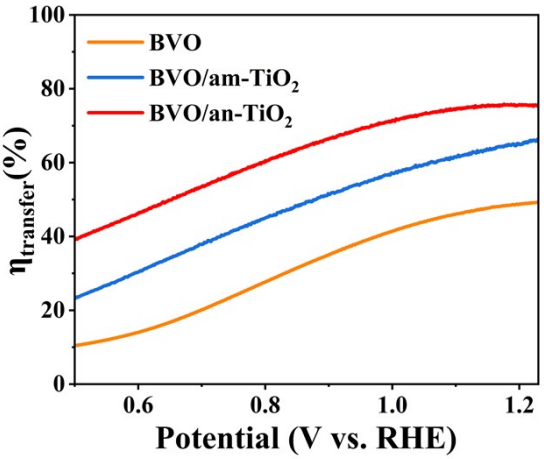

Figure S10 Charge transfer efficiency of BVO, BVO/am-TiO_2, and BVO/an-TiO_2.

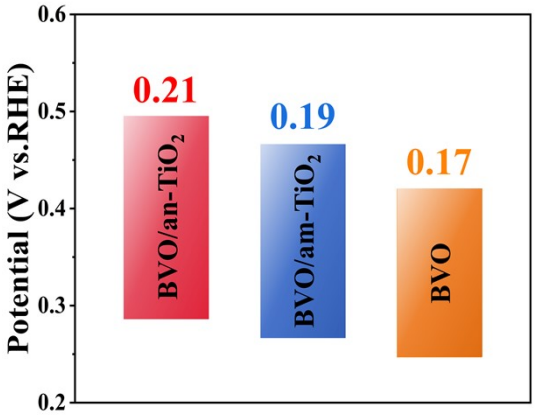

Figure S11 Open-circuit potentials (U_{OC}) measured in the dark and under AM 1.5G illumination.

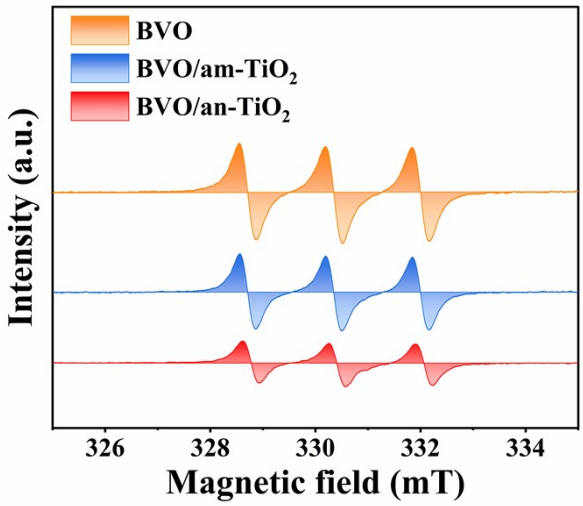

Figure S12 EPR spectra of BVO, BVO/am-TiO_2, and BVO/an-TiO_2 (using TEMPO as probe).

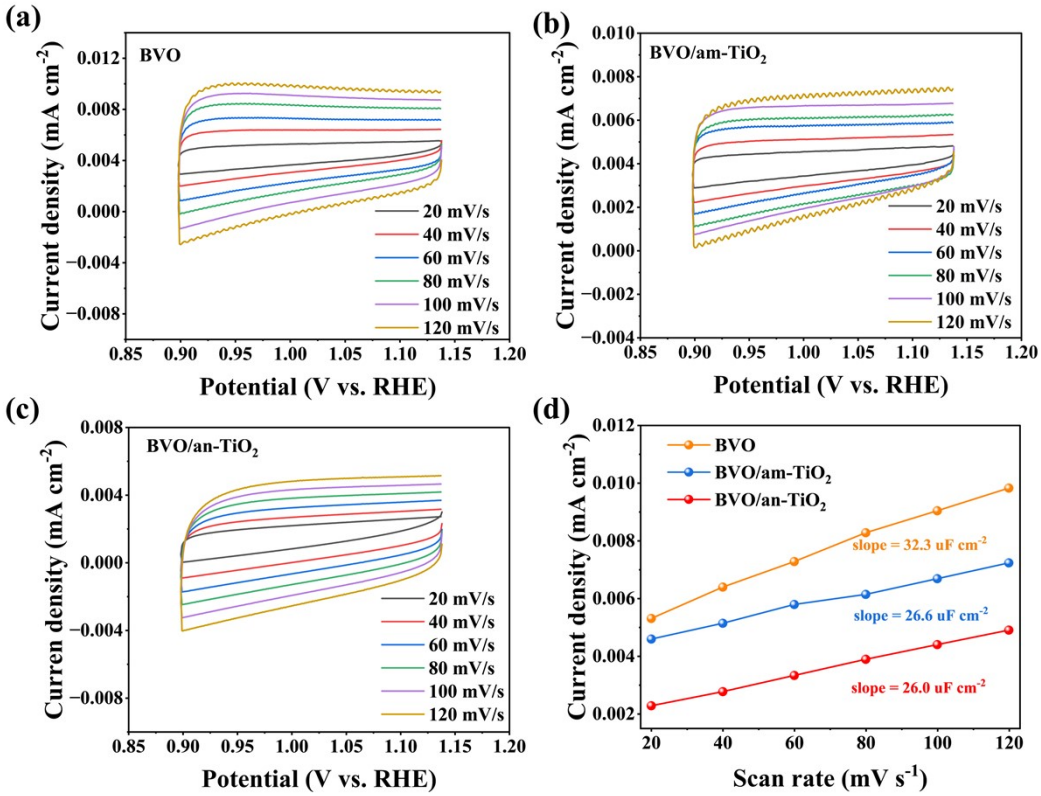

Figure S13 (a)-(c) Cyclic voltammetry tested in the dark for BVO, BVO/am-TiO_2 and BVO/an-TiO_2. (d) Charging current densities recorded at 1.138 V_{RHE} at different scan rates (20, 40, 60, 80, 100, 120 mV/s).

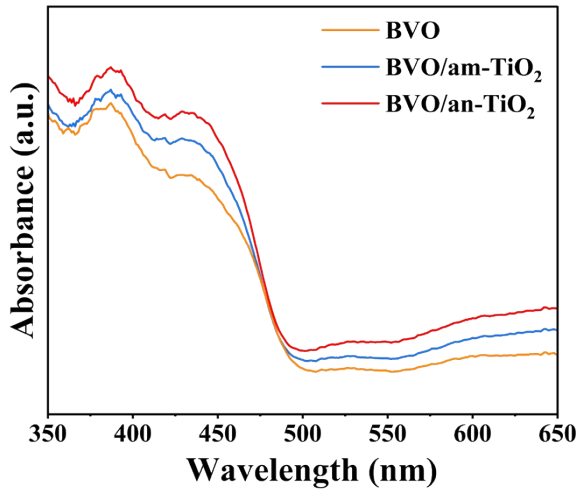

Figure S14 UV-vis spectra of BVO, BVO/am-TiO_2 and BVO/an-TiO_2.

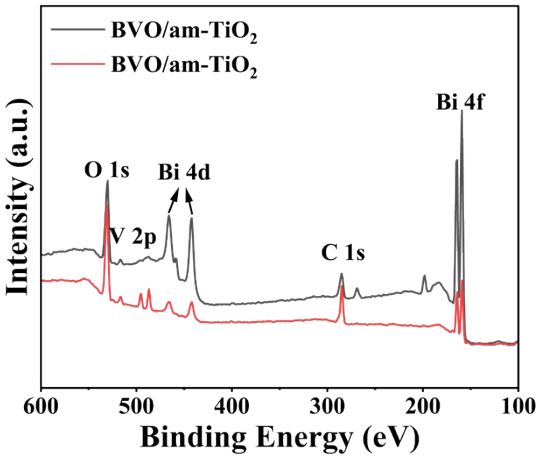

Figure S15 XPS spectra of BVO/am-TiO_2 and BVO/an-TiO_2 photoanodes.

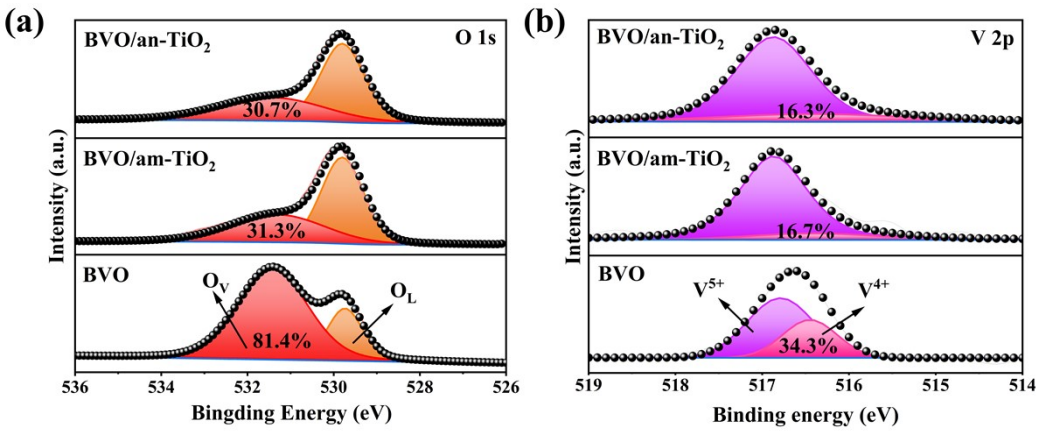

Figure S16 (a) O 1s and (b) V 2p XPS spectra of BVO, BVO/am-TiO_2, and BVO/an-TiO_2.

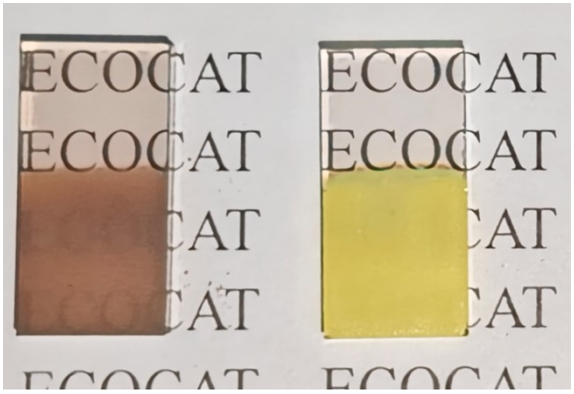

Figure S17 (a) Ta_3N_5/CoOOH photoanode. (b) BVO/an-TiO_2/FeOOH/NiOOH photoanode. Although the $BiVO_4$ film appears non-transparent, it exhibits wavelength-dependent absorption and partial light transmission in the visible region relevant for tandem operation.

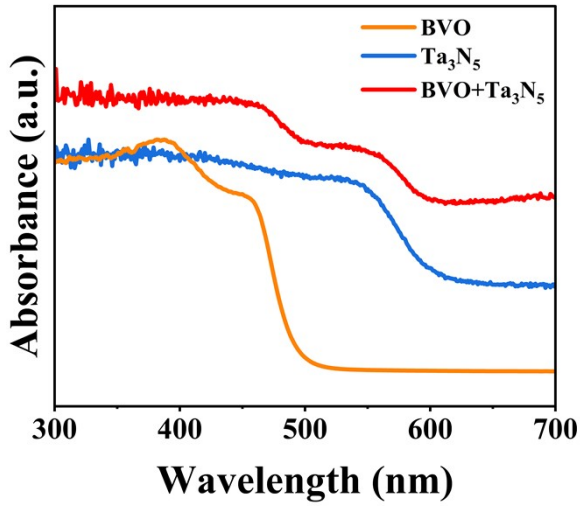

Figure S18 UV-vis spectra of BVO, Ta_3N_5, and BVO||Ta_3N_5 photoanodes.

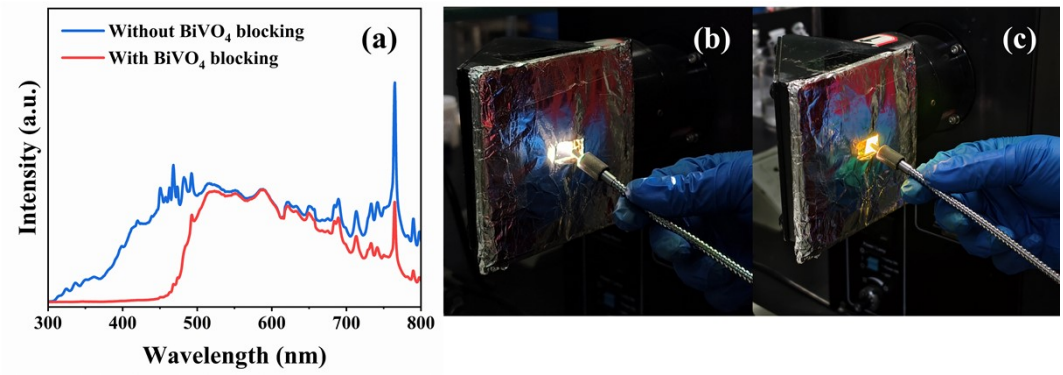

Figure S19 (a) AM 1.5G spectral distribution measured under conditions with and without blocking by the $BiVO_4$ photoanode. (b) Photograph of the AM 1.5G spectral measurement setup without $BiVO_4$ photoanode blocking. (c) Photograph of the AM 1.5G spectral measurement setup with $BiVO_4$ photoanode blocking.

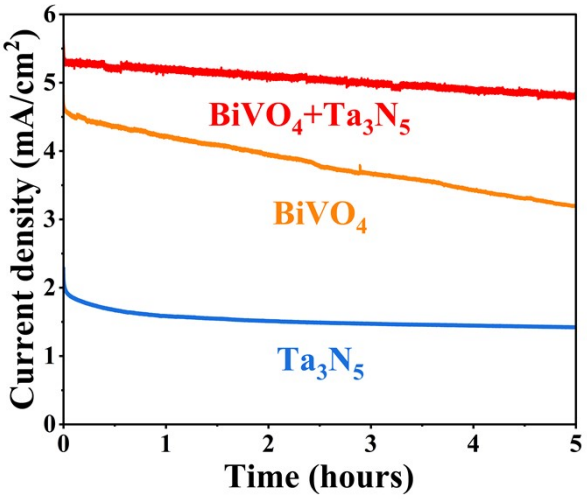

Figure S20 Stability tests of BVO/an-TiO_2/FeOOH/NiOOH, Ta_3N_5/CoOOH, and BVO/an-TiO_2/FeOOH/NiOOH||Ta_3N_5/CoOOH photoanodes. The $BiVO_4$+Ta_3N_5 dual photoanode maintains a higher steady-state photocurrent than $BiVO_4$ and Ta_3N_5 under continuous illumination, consistent with effective tandem operation.

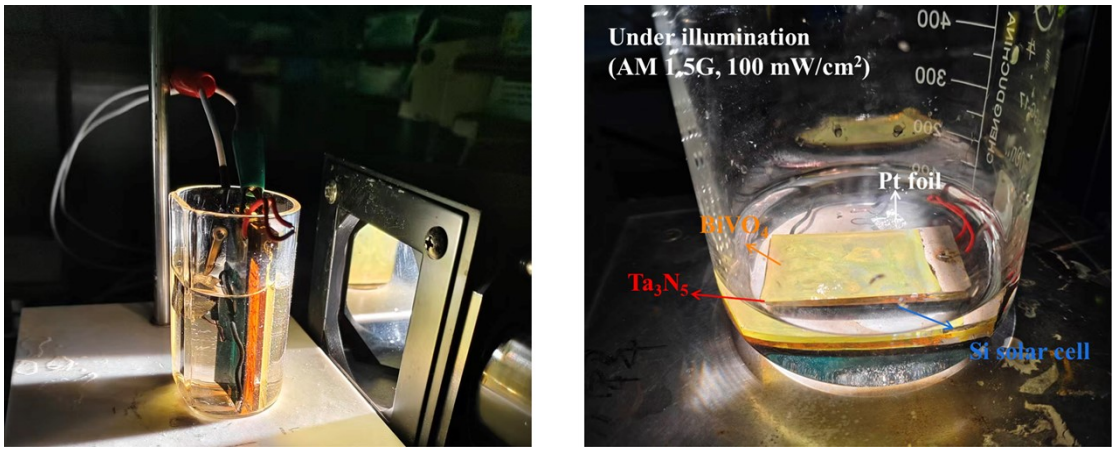

Figure S21 Photos of $BiVO_4$||Ta_3N_5-Si Unassisted PEC water splitting device.

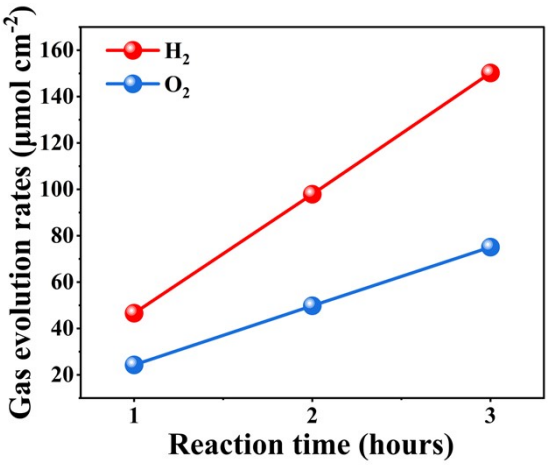

Figure S22 Gas evolution rates from unassisted PEC water splitting at 1.23 V_{RHE}.

Table S2 Comparisons of photoelectrochemical performance (photocurrent density, IPCE, and stability) of BVO/an-TiO_2/FeOOH/NiOOH with other reported BVO photoanodes.

Year	Photoanode	Measurement conditions	Performance at 1.23 V_{RHE}	Maximum IPCE	Stability	Ref.
Present	$BiVO_4$/an-TiO_2/FeOOH/NiOOH	1M K-Bi (pH 9.5)	4.5 mA cm^{-2}	80% at 460 nm	5 h	This work
2023	NiB/$BiVO_4$	0.5 M NaB+Ni^{2+}	6 mA cm^{-2}	95% at 350 nm	600 h	5
2022	E-$BiVO_4$/BPQDs/TiO_2	0.5 M KPi (pH 7)	6.2 mA cm^{-2}	58% at 380nm	50 h	6
2023	$BiVO_4$/PEI/TiO_2 /CoOOH	0.5 M KPi (pH 8.0)	2.03 mA cm^{-2}	92% at 390 nm	400 h	7
2022	$NiFeO_x$/P-$BiVO_4$	0.1 M KPi (pH 7)	4.9 mA cm^{-2}	75% at 410 nm	10 h	8
2024	NiMoFeCoCrOOH/BVO	0.5 M KBi	5.23 mA cm^{-2}	75% at 350 nm	100 h	9
2022	NiFeOx/Cr-BVO	1 M KBi (pH 9)	4.4 mA cm^{-2}	58% at 390 nm	24 h	10
2025	Ov-$BiVO_4$/MIL-101	1 M KBi (pH 9)	5.91 mA cm^{-2}	89% at 390 nm	3.5 h	11
2024	$BiVO_4$/Fe_2TiO_5/MF	1 M KBi buffer (pH 9.5)	3.33 mA cm^{-2}	60% at 460 nm	6 h	12
2025	$BiVO_4$/$NiCo_2O_4$/TiO_2	0.5 M KBi （PH 8.5）	3.62 mA cm^{-2}	68% at 420 nm	9 h	13
2025	CoFe-OEC/TiN/BVO	0.5 M NaBi	5 mA cm^{-2}	80% at 450 nm	5 h	14
2022	NiFe-MOFs/$BiVO_4$	0.5 M K_3BO_3 (pH 9.5)	4.61 mA cm^{-2}	58% at 410 nm	3 h	15
2023	NiOOH/Co_3O_4/$BiVO_4$	1 M KBi	6.4 mA cm^{-2}	91% at 440 nm	90 h	16
2023	$Ni(OH)_2$/Cl-$BiVO_4$	0.5 M K_3BO_3 (pH 9.5)	4.33 mA cm^{-2}	55% at 390 nm	3 h	17
2024	$NiFeO_x$/EBVO-(-150)	1 M KBi (pH 9.5)	6.3 mA cm^{-2}	80% at 400 nm	30 h	18
2024	Cu-RuO_2-Tm-$BiVO_4$	0.5 M Na_2SO_4 (pH 6.4)	5.3 mA cm^{-2}	85% at 420 nm	24 h	19

Table S3 Comparison of representative $BiVO_4$-based unassisted tandem PEC water-splitting systems coupled with non-perovskite photovoltaic devices, with reported STH efficiencies.

Year	System	Electrolyte	STH (%)	Ref.
2025	$BiVO_4$||Ta_3N_5-Si solar cell	1 M KBi	3.1	This work
2020	Fe(Ni)OOH/$BiVO_4$/WO_3/TiO_2 /SiO_X/n Si	0.5 M Kbi (pH 9)	0.25	20
2023	NiFe-LDH/BVO/SnO_2/TTO /TOPCon Si	1 M KBi (pH 9.5)	1.7	21
2023	n-Si/$BiVO_4$ tandem	1 M KBi (pH 9.5)	0.6	22
2023	n^+p-Si/Nb_2O_5/NiPt||W:$BiVO_4$/NiCoO(OH)	1 M KBi (pH 9.5)	3.9	23
2025	Ov-$BiVO_4$/MIL-101-Si solar cell	1 M KPi (pH 9.5)	4.3	11
2020	NiOOH/FeOOH/$BiVO_4$/Pt/SiHJ-Si	1 M KBi (pH 9)	3.5	24

References

1. W. Shockley and H. J. Queisser, *J. Appl. Phys.*, 1961, **32**, 510-519.
2. S. Y. Reece, J. A. Hamel, K. Sung, T. D. Jarvi, A. J. Esswein, J. J. H. Pijpers and D. G. Nocera, *Science*, 2011, **334**, 645-648.
3. B. Khan, M. B. Faheem, K. Peramaiah, J. Nie, H. Huang, Z. Li, C. Liu, K.-W. Huang and J.-H. He, *Nat. Commun.*, 2024, **15**, 6990.
4. Y. Qiu, W. Liu, W. Chen, W. Chen, G. Zhou, P. C. Hsu, R. Zhang, Z. Liang, S. Fan, Y. Zhang and Y. Cui, *Sci. Adv.*, 2016, **2**, e1501764.
5. R. T. Gao, N. T. Nguyen, T. Nakajima, J. L. He, X. H. Liu, X. Y. Zhang, L. Wang and L. M. Wu, *Sci. Adv.*, 2023, **9**, eade4589.
6. B. J. Jin, Y. Cho, C. Park, J. Jeong, S. Kim, J. Jin, W. Kim, L. Y. Wang, S. Y. Lu, S. L. Zhang, S. H. Oh, K. Zhang and J. H. Park, *Energy Environ. Sci.*, 2022, **15**, 672-679.
7. S. Bae, T. Moehl, E. Service, M. Kim, P. Adams, Z. B. Wang, Y. Choi, J. Ryu and S. D. Tilley, *Nat. Commun.*, 2024, **15**, 9439.
8. H. Wu, L. Zhang, A. J. Du, R. Irani, R. van de Krol, F. F. Abdi and Y. H. Ng, *Nat. Commun.*, 2022, **13**, 6231.
9. L. Wang, Z. H. Gao, K. R. Su, N. T. Nguyen, R. T. Gao, J. X. Chen and L. Wang, *Adv. Funct. Mater.*, 2024, **34**, 2315674.
10. Y. J. Jeong, D. H. Seo, J. H. Baek, M. J. Kang, B. N. Kim, S. K. Kim, X. L. Zheng and I. S. Cho, *Adv. Funct. Mater.*, 2022, **32**, 2208196.
11. Y. L. Xin, J. Tian, X. Q. Xiong, C. L. Wu, S. A. C. Carabineiro, X. G. Yang, Z. X. Chen, Y. Xia and Y. X. Jin, *Adv. Mater.*, 2025, **37**, 2417589.
12. Q. J. Wang, L. L. Oldham, A. Giner-Requena, Z. Y. Wang, D. Benetti, S. Montilla-Verdú, R. Chen, D. F. Du, T. Lana-Villarreal, U. Aschauer, N. Guijarro, J. R. Durrant and J. S. Luo, *J. Am. Chem. Soc.*, 2024, **146**, 34681-34689.
13. J. W. Yang, M. N. Chao, Q. Zhao, J. P. Li and G. Liu, *J. Alloys Compd.*, 2025, **1024**, 180186.
14. H. H. Sun, P. Wang, W. Hua, D. Lei, Y. Y. Li and J. G. Wang, *J. Colloid Interface Sci.*, 2025, **689**, 137212.
15. Y. Li, Q. Wang, X. Hu, Y. Meng, H. She, L. Wang, J. Huang and G. Zhu, *Chem. Eng. J.*, 2022, **433**,

133592.

16. Y. Zhang, L. Xu, B. Liu, X. Wang, T. Wang, X. Xiao, S. Wang and W. Huang, *ACS Catal.*, 2023, **13**, 5938-5948.
17. J. Zhang, X. Wei, J. Zhao, Y. Zhang, L. Wang, J. Huang, H. She and Q. Wang, *Chem. Eng. J.*, 2023, **454**, 140081.
18. X. Li, Z. Wang, A. Sasani, A. Baktash, K. Wang, H. Lu, J. You, P. Chen, P. Chen, Y. Bao, S. Zhang, G. Liu and L. Wang, *Nat. Commun.*, 2024, **15**, 9127.
19. K. Tian, L. Jin, A. Mahmood, H. Yang, P. An, J. Zhang, Y. Ji, Y. Li, D. Li, S. Liu and J. Yan, *Adv. Funct. Mater.*, 2024, **34**, 2410548.
20. I. Y. Ahmet, S. Berglund, A. Chemseddine, P. Bogdanoff, R. F. Präg, F. F. Abdi and R. van de Krol, *Adv. Energy Sustain. Res.*, 2020, **1**, 2000037.
21. G. Jung, C. Moon, F. Martinho, Y. Jung, J. Chu, H. Park, A. Hajijafarassar, R. Nielsen, J. Schou, J. Park, P. C. K. Vesborg, O. Hansen, Y. S. Lee, S. Canulescu and B. Shin, *Adv. Energy Mater.*, 2023, **13**, 2301235.
22. S. Wang, S. Feng, B. Liu, Z. Gong, T. Wang and J. Gong, *Chem. Sci.*, 2023, **14**, 2192-2199.
23. M. Arunachalam, R. Subhash Kanase, J. Ganapati Badiger, S. Abdelfattah Sayed, K. S. Ahn, J. S. Ha, S. W. Ryu and S. Hyung Kang, *Chem. Eng. J.*, 2023, **474**, 145262.
24. S. Feng, T. Wang, B. Liu, C. Hu, L. Li, Z. J. Zhao and J. Gong, *Angew. Chem., Int. Ed.*, 2020, **59**, 2044-2048.